ACS NANO

www.acsnano.org

ARTICLE

Engineering Magnetic Phases of Layered Antiferromagnets by Interfacial Charge Transfer

Kaichen Xie, Xiao-Wei Zhang, Di Xiao,* and Ting Cao*

Cite This: *ACS Nano* 2023, 17, 22684–22690

Read Online

ACCESS | Metrics & More | Article Recommendations | Supporting Information

ABSTRACT: **Van der Waals heterostructures composed of distinct layered materials can display behaviors entirely different from those of each individual layer due to interfacial coupling. Here we investigate the manipulation of magnetic phases in two-dimensional magnets through interfacial charge transfer in heterostructures of magnetic and nonmagnetic layers. This is demonstrated by first-principles calculations, which unveil a transition toward the ferromagnetic phase by stacking antiferromagnetic bilayer CrSBr on graphene. Using an effective model consisting of two electronically coupled single layers, we show that the antiferromagnetic to ferromagnetic magnetic phase transition occurs due to interfacial charge transfer, which enhances ferromagnetism. We further reveal that the magnetic phase transition can also be induced by electron and hole carriers and demonstrate that the phase transition is a spin-canting process. This allows for precise gate-control of noncollinear magnetism on demand. Our work predicts interfacial charge transfer as a potent mechanism to tune magnetic phases in van der Waals heterostructures and creates opportunities for spintronic applications.**

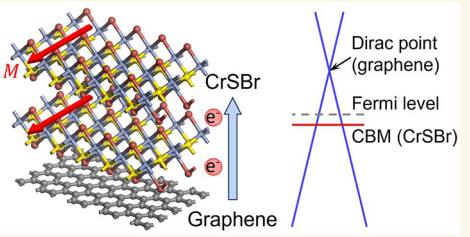

KEYWORDS: *2D magnets, magnetic semiconductors, magnetic phase transition, first-principles calculations, graphene*

Van der Waals (vdW) materials have emerged as a fertile ground for exploring substantial physical phenomena and are highly attractive as a promising class of materials for applications ranging from nanoelectronics and nanophotonics to sensing. One of the most intriguing aspects of vdW materials lies in the ability to manipulate and control their physical properties by precisely adjusting interlayer interactions. This capability has sparked significant interest in the realm of vdW heterostructures and moiré superlattices, leading to discoveries such as the emergence of strongly correlated phases arising from moiré bands and the formation of interlayer excitons trapped in the moiré potential.[1−5] Within the family of vdW materials, two-dimensional (2D) vdW magnets stand out, as they introduce an extra magnetic degree of freedom, which opens up opportunities for engineering vdW interfaces and developing innovative magnetoelectric, magneto-optic, and spintronic devices.[6,7] In vdW magnets, the interlayer exchange, although considerably weaker compared to the intralayer exchange, plays a crucial role in determining the magnetic order of the whole system.[8] Previous studies have demonstrated that the interlayer magnetic interactions can be fine-tuned using a range of methods including magnetic fields, electric fields, doping, strain, pressure, and stacking.[9−18] This extensive tunability offers the possibility for not only uncovering distinct magnetic phases, like noncollinear moiré magnetism,[19−21] but also the creation of compact and energy-efficient spintronic devices.

RESULTS AND DISCUSSION

In this work, we propose a strategy to control the interlayer magnetic interactions by engineering band alignment and charge transfer at the interfaces between vdW magnets and other vdW materials. We select the bilayer CrSBr/monolayer graphene (biCrSBr/G) heterostructure (Figure 1a) as a model platform to demonstrate the controllable interlayer magnetism in CrSBr.

CrSBr is an A-type magnetic semiconductor, where each monolayer is FM, but the neighboring layers are AFM coupled (Figure 1b).[22−26] CrSBr exhibits in-plane magnetic anisotropy along the *b*-axis and a hard axis along the *c*-axis. The Néel temperature of bulk CrSBr is ∼132 K, which is notably higher than that of vdW magnetic semiconductors such as CrX_3 (X = Cl, Br, I) and $Cr_2Ge_2Te_6$.[6,7,27,28] Recently, a reversible strain-

Received: July 31, 2023
Revised: November 8, 2023
Accepted: November 9, 2023
Published: November 14, 2023

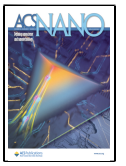

https://doi.org/10.1021/acsnano.3c07125
ACS Nano 2023, 17, 22684−22690

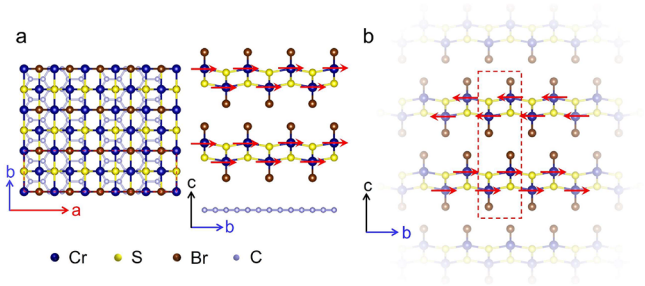

Figure 1. (a) Crystal structure of the bilayer CrSBr/monolayer graphene (biCrSBr/G) heterostructure in a supercell. The CrSBr bilayer is stacked directly on the graphene monolayer with the *a*- and *b*-axes of CrSBr aligned along the armchair and zigzag directions of graphene, respectively. The strain on graphene is <5%. Top and side views are shown on the left and right, respectively. (b) Side-view crystal and magnetic structures for CrSBr, a typical A-type layered van der Waals magnet. The system is ferromagnetic within each layer and antiferromagnetically coupled between neighboring layers. The unit cell is marked by a red dashed rectangular.

induced magnetic phase transition has been observed in bulk CrSBr when subjected to uniaxial strain applied along the *a*-axis.[10] The critical strain for the AFM to FM magnetic phase transition is ∼1% along *a*, as confirmed by both experiments and calculations. This magnetic phase transition is attributed to changes in bond geometry (including bond length and bond angle), which significantly influence the magnitude and sign of magnetic exchange couplings, according to the Goodenough–Kanamori rules.[29−31] Compared with magnetic phase transitions controlled by structural engineering, such as applying strain, pressure, and shifting stacking orders, interfacial charge transfer offers an easier and more universal control knob that can enable robust switching of the interlayer magnetism in 2D magnets.

To calculate the biCrSBr/G heterostructure from first principles, we employ a 5 × 1 supercell of a CrSBr bilayer and an 8 × 2 supercell of a graphene monolayer, resulting in nearly commensurate top and bottom layers (see Methods and Supporting Information, Section I for details). In this supercell, the *a*- and *b*-axes of CrSBr are aligned along the armchair and zigzag directions of graphene, respectively (Figure 1a).

In contrast to its AFM ground state in the freestanding CrSBr bilayer, the calculated ground state of the CrSBr bilayer in the biCrSBr/G heterostructure becomes FM (Figure 1a). The calculated energy difference between the FM and AFM states $\Delta E = E_{FM} - E_{AFM}$, changes from 0.12 meV in the freestanding bilayer to −0.07 meV per unit cell ($Cr_4S_4Br_4$) upon stacking. We note that the calculated ΔE = 0.12 meV for the freestanding bilayer is in good agreement with the experimental measurement of the critical field of 0.134 T along the easy axis *b*, which suggests ΔE = 0.09 meV.[14] We further investigated the electronic properties of the heterostructure. The reciprocal space geometry of monolayer graphene, bilayer CrSBr, and the biCrSBr/G heterostructure is shown in Figure 2a. The corners (labeled K_G) in the hexagonal Brillouin zone (BZ) of graphene unit cells are folded onto the Γ−Y path in the rectangular BZ of the biCrSBr/G heterostructure, marked by K in the shaded rectangular area of Figure 2a. The band structures of the FM biCrSBr/G heterostructure for majority and minority spins are plotted along a BZ *k*-path (Γ−X−S−Y−Γ) in Figure 2b and c, respectively, colored by a layer localization function defined as $\eta_n(\mathbf{k}) = \frac{\sum_{i\in Cr}|\langle\psi_i|\phi_n(\mathbf{k})\rangle|^2 - \sum_{i\in G}|\langle\psi_i|\phi_n(\mathbf{k})\rangle|^2}{\sum_{i\in Cr}|\langle\psi_i|\phi_n(\mathbf{k})\rangle|^2 + \sum_{i\in G}|\langle\psi_i|\phi_n(\mathbf{k})\rangle|^2}$, where *n* is the band index and **k** is the wavevector in reciprocal space. $\phi_n(\mathbf{k})$ and ψ_i denote the electron wave function and active atomic orbital *i* in the top CrSBr bilayer (Cr) or the bottom graphene monolayer (G). Therefore, $\eta_n(\mathbf{k})$ = 1 represents the wave function completely localized in the top CrSBr bilayer, while $\eta_n(\mathbf{k})$ = −1 represents the wave function completely localized in the bottom graphene monolayer, marked by red and blue, respectively. The calculated band alignment between the CrSBr bilayer and graphene monolayer shows that the Dirac point of graphene is higher than the conduction band minimum (CBM) of the CrSBr bilayer by ∼0.5 eV. This suggests significant interfacial charge transfer between the CrSBr bilayer and graphene monolayer, and the electron density transferred from the graphene monolayer to the CrSBr bilayer is estimated to be ∼2.1 × 10^{13}/cm^2 from Luttinger's theorem.[32,33]

To investigate the origin of the magnetic phase transition upon stacking and whether the transition arises from the interfacial charge transfer, we calculate the carrier doping dependent ΔE between the collinear FM and AFM states for CrSBr bilayers without graphene. Figure 3a shows that ΔE decreases almost linearly with increasing carrier density for both electron and hole, in the small carrier density regime (<3

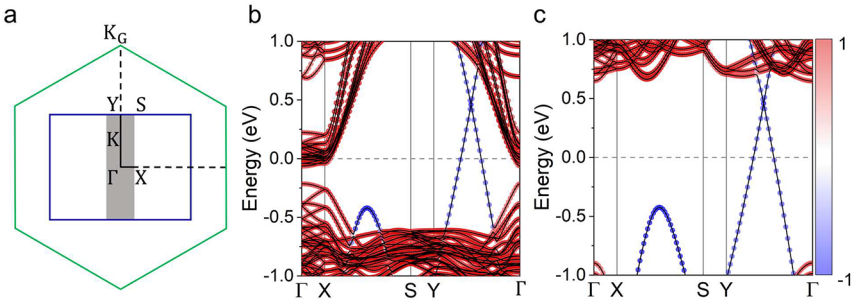

Figure 2. (a) Schematic of the Brillouin zone (BZ) of graphene (green hexagon), CrSBr (blue rectangle), and the biCrSBr/G supercell (gray-shaded rectangle). The Dirac point (K_G) in the hexagonal BZ of the graphene unit cell is folded onto the Γ−Y path in the rectangular BZ of the biCrSBr/G heterostructure (marked by K). (b, c) Calculated Kohn−Sham band structures of the ferromagnetic biCrSBr/G heterostructure for (b) majority and (c) minority spins, respectively. The band wave function projection in CrSBr and graphene layers is marked by red and blue, respectively (see exact definition in the main text). The Fermi level is shown by gray dashed lines. The charge transfer between the CrSBr/graphene interface is ∼2.1 × 10^{13}/cm^2 from calculations.

https://doi.org/10.1021/acsnano.3c07125
ACS Nano 2023, 17, 22684−22690

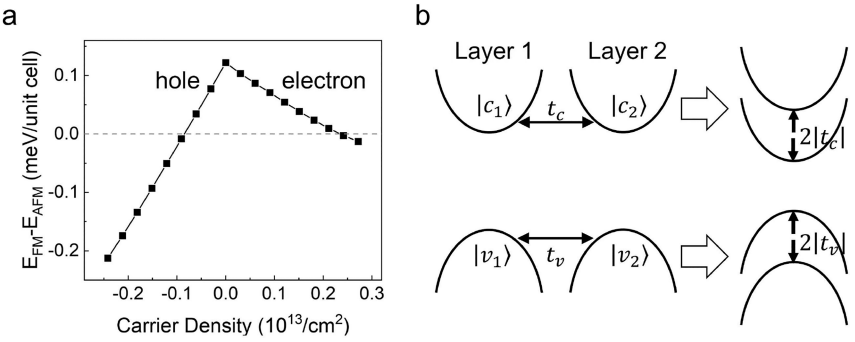

Figure 3. (a) Doping-dependent energy difference between collinear ferromagnetic and antiferromagnetic bilayer CrSBr ($\Delta E = E_{FM} - E_{AFM}$). Positive (negative) carrier density refers to a doped electron (hole) carrier density. Lines are guides to the eye. The AFM to FM magnetic phase transition occurs for both electron and hole doping. (b) Schematic illustration of interlayer coupling in layered van der Waals magnets. Two neighboring layers are labeled by layer 1 and layer 2, with states $|c_1\rangle$, $|v_1\rangle$ and $|c_2\rangle$, $|v_2\rangle$ schematically shown by parabolic bands. t_c and t_v denote the interlayer hopping between degenerate conduction and valence bands, respectively. With interlayer hybridization, $|c_1\rangle$ and $|c_2\rangle$ form bonding and antibonding orbitals with energy difference $2|t_c|$, while $|v_1\rangle$ and $|v_2\rangle$ form bonding and antibonding orbitals with energy difference $2|t_v|$.

$\times 10^{12}$/cm^2). This behavior suggests that both electron and hole doping favor the collinear FM phase over the AFM phase, and the doping leads to an AFM to FM magnetic phase transition. In CrSBr bilayers, the critical carrier density at phase transition for hole doping (0.8×10^{12}/cm^2) is much smaller than that for electron doping (2.4×10^{12}/cm^2). Nonetheless, in the biCrSBr/G heterostructure, the electron carrier density in the CrSBr bilayer due to interfacial charge transfer ($\sim 2.1 \times 10^{13}$/cm^2) is an order of magnitude larger than the critical density. We therefore attribute the ferromagnetism in the biCrSBr/G heterostructure to the interfacial charge transfer thanks to the band alignment between the two materials.

To further exploit and control the magnetic phase transitions from interfacial charge transfer, we use open-shell molecules (e.g., NO_2) as admolecules to introduce charge carriers. We find an FM magnetic ground state of the CrSBr bilayer with NO_2 adsorption at a density of 1.1×10^{-10} mol/cm^2 (see Supporting Information, Section II for details). This provides another route to achieve reversible magnetic phase transition in 2D magnets by molecular adsorption, as the initial undoped state can be recovered by annealing.[34]

To unveil the physical mechanism and general design strategy of magnetic phase transitions enabled by charge transfer, we construct an effective model consisting of ferromagnetic layers being electronically coupled, to describe layered A-type magnetic semiconductors including $MnBi_2Te_4$, CrX3, CrSBr, and $CrPS_4$.[13,23,27,35−37] The key to carrier doping induced ferromagnetism lies in the interlayer electronic coupling, i.e., electron (hole) hopping across the vdW interfaces. In this model, we include the frontier conduction bands (i.e., $|c_1(\mathbf{k})\rangle$ and $|c_2(\mathbf{k})\rangle$) or valence bands (i.e., $|v_1(\mathbf{k})\rangle$ and $|v_2(\mathbf{k})\rangle$) in the two adjacent layers as the basis (layer 1 and layer 2 in Figure 3b). $E = E_c(\mathbf{k})$ or $E_v(\mathbf{k})$ is the eigenenergy of the corresponding frontier conduction or valence bands in each monolayer, respectively. $t = t_c(\mathbf{k})$ or $t_v(\mathbf{k})$ denotes the $\mathbf{k}$-dependent interlayer hopping between the degenerate conduction or valence bands, respectively. Considering the interlayer wave function hybridization between these originally degenerate frontier bands, the Hamiltonian reads

$$H(\mathbf{k}) = \begin{pmatrix} E(\mathbf{k}) & t(\mathbf{k}) \\ t(\mathbf{k}) & E(\mathbf{k}) \end{pmatrix} \quad (1)$$

By solving the Hamiltonian in eq 1, bonding and antibonding states can be obtained as $E_{\pm}(\mathbf{k}) = E(\mathbf{k}) \pm t(\mathbf{k})$ (Figure 3b). Therefore, with interlayer hybridization, $|c_1(\mathbf{k})\rangle$ and $|c_2(\mathbf{k})\rangle$ form bonding and antibonding orbitals with energy difference $2|t_c(\mathbf{k})|$, while $|v_1(\mathbf{k})\rangle$ and $|v_2(\mathbf{k})\rangle$ form bonding and antibonding orbitals with energy difference $2|t_v(\mathbf{k})|$.

The charge transfer process in the biCrSBr/G heterostructure can be treated equivalently as the introduction of carriers into a layered magnetic semiconductor. In the context of dilute doping, the energy difference between the FM and AFM phases changes by $-|(t_{FM} - t_{AFM})n|$, where hopping is evaluated at $\mathbf{k} = 0$. Here, n represents the number of charge carriers introduced to the system and is measured by carrier density (cm^{-2}) for 2D materials in Figure 3a. Furthermore, we argue that $t_{AFM} \sim 0$, as the interlayer hybridization between degenerate states in adjacent layers is suppressed by the interlayer AFM order. This suppression happens when spin−orbit coupling is weak, and the spinor of the frontier band wave function is layer-polarized to the magnetization direction. As a result,

$$\Delta E(n) = \Delta E(n = 0) - |t_{FM} n| \quad (2)$$

Here, $t_{FM} = t_c(\mathbf{k} = 0)$ and $t_v(\mathbf{k} = 0)$ for electron and hole doping an FM bilayer, respectively. This effective model correctly reproduces the linear dependence of ΔE with carrier density from DFT calculations (Figure 3a). The slight decrease in the absolute value of the slope observed with increasing carrier density possibly results from the change in the interlayer hopping with k. ΔE can be affected by additional factors, such as the interlayer electric polarization, which has not been included in the present model. Nonetheless, the FM state remains more stable than the AFM state at the high doping levels of biCrSBr/G. We note that the super-super-exchange interaction J that dictates $\Delta E(n = 0)$ is assumed to remain unchanged by doping, which applies to the dilute doping limit as we will show the next.

Based on the model we have developed for doping-induced magnetic phase transition in 2D layered magnets, the interlayer hopping at the FM state can be extracted from Figure 3a. By analyzing the slopes of ΔE vs carrier density curves, we obtain $t^c_{FM} = 31$ meV and $t^v_{FM} = 84$ meV in accordance with eq 2 for the bilayer CrSBr unit cell ($Cr_4S_4Br_4$). We further validate our effective model by comparing its parameters to the hopping

https://doi.org/10.1021/acsnano.3c07125
ACS Nano 2023, 17, 22684−22690

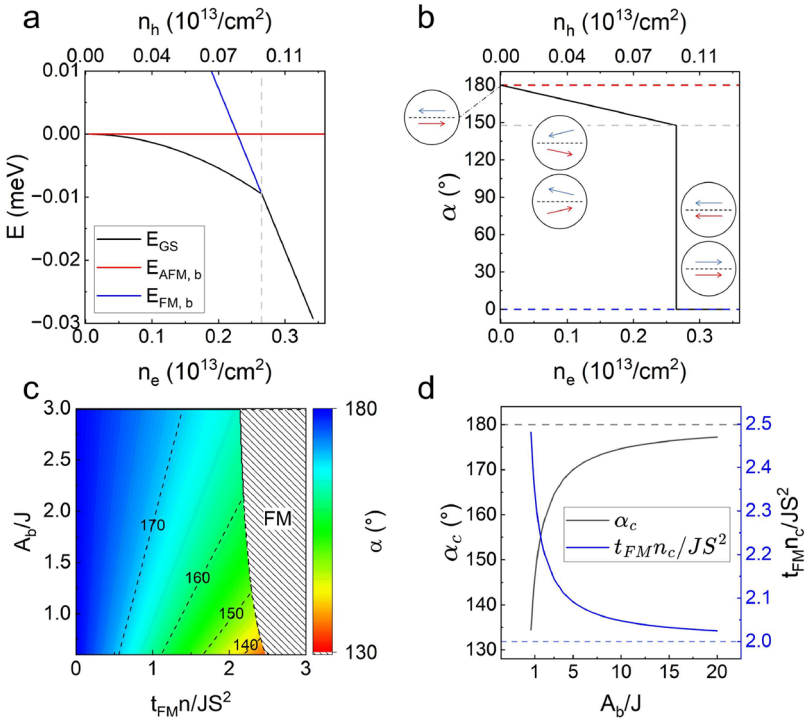

Figure 4. Carrier doping induced magnetic phase transition with noncollinear spins. (a) Carrier density (n_e and n_h for electron and hole, respectively) dependent ground-state energy E_{GS} (black solid line) for bilayer CrSBr. The energies of AFM ($E_{AFM,b}$) and FM ($E_{AFM,b}$) states with spins collinear to the easy axis are plotted in red and blue solid lines for reference, with $E_{AFM,b}$ set to 0. The critical doping density is represented by a gray dashed line. (b) Carrier density dependent canting angle between spins of neighboring layers for bilayer CrSBr. The corresponding spin configurations are shown schematically by insets. The critical angle is shown by a gray dashed line. (c) Doping- and anisotropy-dependent canting angle between spins of neighboring layers in hard-axis A-type 2D magnets. $t_{FM}n/JS^2$ and A_b/J reflect the effects of doping and anisotropy, respectively. (d) Anisotropy-dependent critical angle (left) and critical carrier density (right).

obtained from the DFT bands. From DFT band splitting, we obtain $t^c_{AFM} = t^v_{AFM} = 0$ and $t^c_{FM} = 31$ meV, $t^v_{FM} = 76$ meV, which agree reasonably well with those obtained based on the effective model (see Supporting Information, Sections III and IV for details). This agreement indicates that the model correctly describes the microscopic mechanism of magnetic phase transition and validates the assumption that the change of interlayer super-super exchange between localized Cr moments can be considered negligible with doping. We further compare band structures with and without carrier doping and confirm that the interlayer hopping for both AFM and FM CrSBr bilayers remains almost unchanged at the DFT level with a small amount of carrier doping (see Supporting Information, Section IV for details). The strategy and model developed here can serve as a general approach for carrier-induced tunable interlayer magnetic order beyond the biCrSBr/G heterostructure.

In anisotropic magnets, AFM to FM phase transitions (with magnetic field, strain, etc.) can happen with antiparallel magnetic moments continuously aligned to parallel or suddenly flipped to parallel. To investigate which process occurs with carrier doping, we explicitly include interlayer exchange interactions and intralayer magnetic anisotropy in the total energy. Without loss of generality, we take triaxial anisotropy into account. The easy axis is set along *b*, following CrSBr. The carrier density dependent total energy per $Cr_2S_2Br_2$ is given by

$$E(n) = J\mathbf{S}_1\cdot\mathbf{S}_2 + \sum_{i=1,2} A_a(\mathbf{S}_i\cdot\hat{a})^2 - A_b(\mathbf{S}_i\cdot\hat{b})^2 + A_c(\mathbf{S}_i\cdot\hat{c})^2 - |tn| \quad (3)$$

Here, the first term refers to the interlayer magnetic exchange coupling, and $J > 0$ favors interlayer AFM states. $\mathbf{S}_1$ and $\mathbf{S}_2$ denote the spins of the neighboring layers. The orientations of $\mathbf{S}_1$ and $\mathbf{S}_2$ are denoted by their tilt angles θ_1 and θ_2 with respect to the *b*-axis and azimuthal angles ϕ_1 and ϕ_2 with respect to the *c*-axis, respectively. The second term describes the anisotropy energies, where $\hat{b}$, $\hat{a}$, and $\hat{c}$ are the easy, intermediate, and hard axes, respectively. For convenience, we set $A_a = 0$ and $A_{b,c} > 0$. The third term is from interlayer hopping of doped electrons (holes), as we discussed previously. The hopping integral $t = t_{FM}\cos(\alpha/2)$, where $\alpha(\theta_1, \theta_2, \phi_1, \phi_2)$ is the angle between $\mathbf{S}_1$ and $\mathbf{S}_2$. The cosine form in t comes from the inner product of spinor wave functions across the vdW interface.[38,39]

We discover that the carrier-induced AFM-to-FM phase transition is always a spin-canting process. This can be understood at the small canting angle limit of eq 3, in which the energy gain from the last term is $\sim\delta\alpha$, whereas the energy penalty from other terms is $\sim(\delta\alpha)^2$. To determine the exact spin configuration and magnetic ground-state energy, we minimize E at each n by taking the partial derivative of eq 3,

$$\frac{\partial E}{\partial\theta_1} = \frac{\partial E}{\partial\theta_2} = \frac{\partial E}{\partial\phi_1} = \frac{\partial E}{\partial\phi_2} = 0 \quad (4)$$

https://doi.org/10.1021/acsnano.3c07125
ACS Nano 2023, 17, 22684−22690

For bilayer CrSBr, we use J = 0.013 meV, A_b = 0.014 meV, and A_c = 0.038 meV obtained from DFT calculations, which are consistent with those fitted from experiments.[40] t_{FM}^{c} = 31 meV and t_{FM}^{v} = 84 meV are extracted from DFT results in accordance with eq 2 as shown above. The dependence of the ground-state energy on carrier density is plotted in Figure 4a, and the energies of easy-axis collinear AFM and FM states are also calculated for comparison. With increasing carrier density, the ground-state energy varies smoothly until a sudden change of slope at a critical carrier density n_c, which is given by $t_{FM}n_c = 4S^2\sqrt{J + A_b}\,(\sqrt{J + A_b} - \sqrt{A_b})$. Therefore, we obtain $n_c^e \sim 2.6 \times 10^{12}/\mathrm{cm}^2$ and $n_c^h \sim 1.0 \times 10^{12}/\mathrm{cm}^2$ for transitioning into FM in the cases of electron and hole doping, respectively. To understand the structures of $\mathbf{S}_1$ and $\mathbf{S}_2$ during this process, we plot $\alpha(n)$ in Figure 4b. With increasing carrier density, the originally antiparallel $\mathbf{S}_1$ and $\mathbf{S}_2$ gradually tilt away from the easy axis (b-axis) in the ab-plane until $n = n_c$. In the canting process, $\mathbf{S}_1$ and $\mathbf{S}_2$ become noncollinear but remain symmetric to the intermediate axis (a-axis). At $n = n_c$, the system suddenly transits to the FM state with $\mathbf{S}_1$ and $\mathbf{S}_2$ aligned along the easy axis. For bilayer CrSBr, the critical transition occurs at $\alpha_c \sim 147°$. This doping-induced spin-canting transition process in bilayer CrSBr is further validated by DFT calculations with spin−orbit coupling included (see Supporting Information, Section V for details).

We expand the discussion to generic A-type 2D magnets with different hard axis anisotropy and interlayer hopping in which the range of canting angles can be significantly different. In accordance with eq 3, the canting angle is controlled by two independent and unitless parameters, $t_{FM}n/JS^2$ and A_b/J. Here we focus only on systems with A_b and J comparable in magnitude. Our results in Figure 4c show that, for systems with weak anisotropy and strong interlayer coupling, spins of neighboring layers can develop a very large canting angle. Figure 4d illustrates the role of magnetic anisotropy in the critical angle and critical carrier density. For systems with large anisotropy ($A_b \gg J$), the magnetic phase transition will approach a spin-flip transition at $t_{FM}n_c \sim 2JS^2$.

CONCLUSIONS

In summary, we have proposed heterostructures consisting of vdW magnets and nonmagnetic layered materials for controlling interlayer magnetism in 2D magnets and demonstrated that carrier doping gives dominant contributions to the tunability of interlayer magnetism in heterostructures with proper band alignment through first-principles calculations. This holds true for not only type-III heterojunctions with the magnetic layers but also metals of which the Fermi level is higher than the CBM or lower than the valence band minimum (VBM) of the magnetic layers. We have built an effective model to elaborate the interlayer hopping difference between the interlayer AFM and FM states as the underlying physical mechanism for the AFM to FM magnetic phase transition observed with both electron and hole doping. By including magnetic anisotropy in our model, we have found that the doping-induced AFM to FM transition is a spin-canting process with critical carrier density. Besides interfacial charge transfer in heterostructures, electrostatic doping can be achieved through molecular adsorption or gating, making it an accessible and effective method to control interlayer magnetism in experiments. Our findings not only provide a general framework for understanding charge transfer induced magnetic phase transition in vdW magnets but also offer a versatile approach to modulating magnetism in 2D magnets via interfacial charge transfer, which opens up opportunities for realizing spintronics at the atomically thin level.

METHODS

Ab initio calculations were performed using DFT implemented in the QUANTUM ESPRESSO package.[41] Norm-conserving pseudopotentials with a plane-wave energy cutoff of 85 Ry were employed.[42] For structural relaxation, we employed the spin-polarized Perdew−Burke−Ernzerhof exchange−correlation functional with van der Waals corrections (PBE-D2).[43] The structures were fully relaxed until the force on each atom was <0.005 eV/Å. The lattice constants along the a- and b-axes were calculated to be 3.511 and 4.712 Å, respectively, and the interlayer distance (Cr−Cr) was calculated to be 8.090 Å in bilayer CrSBr. The lattice constant a was relaxed to 2.457 Å in monolayer graphene. The biCrSBr/G heterostructure was constructed with a 5 × 1 CrSBr supercell stacked on top of an 8 × 2 graphene supercell, where the a- and b-axes of the CrSBr bilayer are aligned along the armchair and zigzag directions of the graphene monolayer, respectively. The graphene monolayer experiences tensile strain of ∼3% along the armchair direction and compressive strain of ∼4% along the zigzag direction. We note that the strain is introduced to ensure a commensurate structure in supercell calculations, and graphene can hardly sustain compressive strain without buckling.[44] However, as the AFM to FM phase transition results from charge transfer, the phase transition should remain robust for an arbitrary stacking geometry between bilayer CrSBr and graphene. The vdW spatial gap between the bottom CrSBr layer (from bottom Br atoms) and the graphene monolayer is 3.380 Å. A vacuum region of 15 Å was added in the out-of-plane direction to avoid interactions between periodic images. An 8 × 30 × 1 k-grid was used for Brillouin zone sampling in the biCrSBr/G heterostructure. A dipole correction was applied in all the calculations for biCrSBr/G heterostructures.[45] The band structures and ground-state energies for each carrier density with electron (hole) doping were calculated within the local spin density approximation (LSDA). The carrier density was tuned by changing the total number of electrons in the unit cell, with a compensating jellium background of opposite charge. A 120 × 90 × 1 k-grid was used for Brillouin zone sampling to converge the magnetic moment at the dilute doping (in a bilayer unit cell without graphene). For magnetic anisotropy, spin−orbit coupling was included at the fully relativistic level. A Gaussian smearing of 1 meV was adopted for electron occupation.

ASSOCIATED CONTENT

Supporting Information

The Supporting Information is available free of charge at https://pubs.acs.org/doi/10.1021/acsnano.3c07125.

The band alignment between the CrSBr bilayer and strained graphene monolayer, calculations for open-shell molecule adsorption induced magnetic phase transition in the CrSBr bilayer, the orbital composition of the first several conduction and valence bands in CrSBr bilayer, Kohn−Sham band structures with charge carriers, and the spin-canting transition from DFT calculations (PDF)

AUTHOR INFORMATION

Corresponding Authors

Di Xiao − *Department of Materials Science and Engineering and Department of Physics, University of Washington, Seattle, Washington 98195, United States*; Email: dixiao@uw.edu

Ting Cao − *Department of Materials Science and Engineering, University of Washington, Seattle, Washington 98195, United*

https://doi.org/10.1021/acsnano.3c07125
ACS Nano 2023, 17, 22684−22690

States; orcid.org/0000-0003-1300-6084;
Email: tingcao@uw.edu

Authors

Kaichen Xie − *Department of Materials Science and Engineering, University of Washington, Seattle, Washington 98195, United States;* orcid.org/0000-0001-8479-8301

Xiao-Wei Zhang − *Department of Materials Science and Engineering, University of Washington, Seattle, Washington 98195, United States*

Complete contact information is available at:
https://pubs.acs.org/10.1021/acsnano.3c07125

Notes

The authors declare no competing financial interest.

ACKNOWLEDGMENTS

The first-principles calculations of two-dimensional magnetic materials were supported by the University of Washington Molecular Engineering Materials Center (DMR-2308979). The theoretical model of doping-dependent magnetism is supported by AFOSR MURI 2D MAGIC (FA9550-19-1-0390). T.C. would like to thank Daniel Rizzo for helpful discussions. K.X. would like to thank Yafei Ren for helpful discussions on theoretical interpretations. This work was facilitated through the use of advanced computational, storage, and networking infrastructure provided by the Hyak supercomputer system and funded by the University of Washington Molecular Engineering Materials Center at the University of Washington.

REFERENCES

(1) Bistritzer, R.; MacDonald, A. H. Moiré Bands in Twisted Double-Layer Graphene. *Proc. Natl. Acad. Sci. U. S. A.* **2011**, *108*, 12233−12237.
(2) Cao, Y.; Fatemi, V.; Fang, S.; Watanabe, K.; Taniguchi, T.; Kaxiras, E.; Jarillo-Herrero, P. Unconventional Superconductivity in Magic-Angle Graphene Superlattices. *Nature* **2018**, *556*, 43−50.
(3) Cao, Y.; Fatemi, V.; Demir, A.; Fang, S.; Tomarken, S. L.; Luo, J. Y.; Sanchez-Yamagishi, J. D.; Watanabe, K.; Taniguchi, T.; Kaxiras, E.; Ashoori, R. C.; Jarillo-Herrero, P. Correlated Insulator Behaviour at Half-Filling in Magic-Angle Graphene Superlattices. *Nature* **2018**, *556*, 80−84.
(4) Wilson, N. P.; Yao, W.; Shan, J.; Xu, X. Excitons and Emergent Quantum Phenomena in Stacked 2D Semiconductors. *Nature* **2021**, *599*, 383−392.
(5) Mak, K. F.; Shan, J. Semiconductor Moiré Materials. *Nat. Nanotechnol.* **2022**, *17*, 686−695.
(6) Huang, B.; Clark, G.; Navarro-Moratalla, E.; Klein, D. R.; Cheng, R.; Seyler, K. L.; Zhong, D.; Schmidgall, E.; McGuire, M. A.; Cobden, D. H.; Yao, W.; Xiao, D.; Jarillo-Herrero, P.; Xu, X. Layer-Dependent Ferromagnetism in a van Der Waals Crystal down to the Monolayer Limit. *Nature* **2017**, *546*, 270−273.
(7) Gong, C.; Li, L.; Li, Z.; Ji, H.; Stern, A.; Xia, Y.; Cao, T.; Bao, W.; Wang, C.; Wang, Y.; Qiu, Z. Q.; Cava, R. J.; Louie, S. G.; Xia, J.; Zhang, X. Discovery of Intrinsic Ferromagnetism in Two-Dimensional van Der Waals Crystals. *Nature* **2017**, *546*, 265−269.
(8) Gibertini, M.; Koperski, M.; Morpurgo, A. F.; Novoselov, K. S. Magnetic 2D Materials and Heterostructures. *Nat. Nanotechnol.* **2019**, *14*, 408−419.
(9) Sivadas, N.; Okamoto, S.; Xu, X.; Fennie; Craig, J.; Xiao, D. Stacking-Dependent Magnetism in Bilayer CrI3. *Nano Lett.* **2018**, *18*, 7658−7664.
(10) Cenker, J.; Sivakumar, S.; Xie, K.; Miller, A.; Thijssen, P.; Liu, Z.; Dismukes, A.; Fonseca, J.; Anderson, E.; Zhu, X.; Roy, X.; Xiao, D.; Chu, J.-H.; Cao, T.; Xu, X. Reversible Strain-Induced Magnetic Phase Transition in a van Der Waals Magnet. *Nat. Nanotechnol.* **2022**, *17*, 256−261.
(11) Huang, B.; Clark, G.; Klein, D. R.; MacNeill, D.; Navarro-Moratalla, E.; Seyler, K. L.; Wilson, N.; McGuire, M. A.; Cobden, D. H.; Xiao, D.; Yao, W.; Jarillo-Herrero, P.; Xu, X. Electrical Control of 2D Magnetism in Bilayer CrI3. *Nat. Nanotechnol.* **2018**, *13*, 544−548.
(12) Li, S.; Ye, Z.; Luo, X.; Ye, G.; Kim, H. H.; Yang, B.; Tian, S.; Li, C.; Lei, H.; Tsen, A. W.; Sun, K.; He, R.; Zhao, L. Magnetic-Field-Induced Quantum Phase Transitions in a van Der Waals Magnet. *Phys. Rev. X* **2020**, *10*, No. 011075.
(13) Peng, Y.; Ding, S.; Cheng, M.; Hu, Q.; Yang, J.; Wang, F.; Xue, M.; Liu, Z.; Lin, Z.; Avdeev, M.; Hou, Y.; Yang, W.; Zheng, Y.; Yang, J. Magnetic Structure and Metamagnetic Transitions in the van Der Waals Antiferromagnet CrPS4. *Adv. Mater.* **2020**, *32*, No. 2001200.
(14) Wilson, N. P.; Lee, K.; Cenker, J.; Xie, K.; Dismukes, A. H.; Telford, E. J.; Fonseca, J.; Sivakumar, S.; Dean, C.; Cao, T.; Roy, X.; Xu, X.; Zhu, X. Interlayer Electronic Coupling on Demand in a 2D Magnetic Semiconductor. *Nat. Mater.* **2021**, *20*, 1657−1662.
(15) Klein, J.; Pingault, B.; Florian, M.; Heißenbüttel, M.-C.; Steinhoff, A.; Song, Z.; Torres, K.; Dirnberger, F.; Curtis, J. B.; Weile, M.; Penn, A.; Deilmann, T.; Dana, R.; Bushati, R.; Quan, J.; Luxa, J.; Sofer, Z.; Alù, A.; Menon, V. M.; Wurstbauer, U.; Rohlfing, M.; Narang, P.; Lončar, M.; Ross, F. M. The Bulk van Der Waals Layered Magnet CrSBr Is a Quasi-1D Material. *ACS Nano* **2023**, *17*, 5316−5328.
(16) Jiang, S.; Li, L.; Wang, Z.; Mak, K. F.; Shan, J. Controlling Magnetism in 2D CrI3 by Electrostatic Doping. *Nat. Nanotechnol.* **2018**, *13*, 549−553.
(17) Song, T.; Fei, Z.; Yankowitz, M.; Lin, Z.; Jiang, Q.; Hwangbo, K.; Zhang, Q.; Sun, B.; Taniguchi, T.; Watanabe, K.; McGuire, M. A.; Graf, D.; Cao, T.; Chu, J.-H.; Cobden, D. H.; Dean, C. R.; Xiao, D.; Xu, X. Switching 2D Magnetic States via Pressure Tuning of Layer Stacking. *Nat. Mater.* **2019**, *18*, 1298−1302.
(18) Chen, W.; Sun, Z.; Wang, Z.; Gu, L.; Xu, X.; Wu, S.; Gao, C. Direct Observation of van Der Waals Stacking−Dependent Interlayer Magnetism. *Science* **2019**, *366*, 983−987.
(19) Hejazi, K.; Luo, Z.-X.; Balents, L. Noncollinear Phases in Moiré Magnets. *Proc. Natl. Acad. Sci. U. S. A.* **2020**, *117*, 10721−10726.
(20) Wang, C.; Gao, Y.; Lv, H.; Xu, X.; Xiao, D. Stacking Domain Wall Magnons in Twisted van Der Waals Magnets. *Phys. Rev. Lett.* **2020**, *125*, No. 247201.
(21) Xu, Y.; Ray, A.; Shao, Y.-T.; Jiang, S.; Lee, K.; Weber, D.; Goldberger, J. E.; Watanabe, K.; Taniguchi, T.; Muller, D. A.; Mak, K. F.; Shan, J. Coexisting Ferromagnetic−Antiferromagnetic State in Twisted Bilayer CrI3. *Nat. Nanotechnol.* **2022**, *17*, 143−147.
(22) Telford, E. J.; Dismukes, A. H.; Lee, K.; Cheng, M.; Wieteska, A.; Bartholomew, A. K.; Chen, Y.-S.; Xu, X.; Pasupathy, A. N.; Zhu, X.; Dean, C. R.; Roy, X. Layered Antiferromagnetism Induces Large Negative Magnetoresistance in the van Der Waals Semiconductor CrSBr. *Adv. Mater.* **2020**, *32*, No. 2003240.
(23) Lee, K.; Dismukes, A. H.; Telford, E. J.; Wiscons, R. A.; Wang, J.; Xu, X.; Nuckolls, C.; Dean, C. R.; Roy, X.; Zhu, X. Magnetic Order and Symmetry in the 2D Semiconductor CrSBr. *Nano Lett.* **2021**, *21*, 3511−3517.
(24) Jiang, Z.; Wang, P.; Xing, J.; Jiang, X.; Zhao, J. Screening and Design of Novel 2D Ferromagnetic Materials with High Curie Temperature above Room Temperature. *ACS Appl. Mater. Interfaces* **2018**, *10*, 39032−39039.
(25) Guo, Y.; Zhang, Y.; Yuan, S.; Wang, B.; Wang, J. Chromium Sulfide Halide Monolayers: Intrinsic Ferromagnetic Semiconductors with Large Spin Polarization and High Carrier Mobility. *Nanoscale* **2018**, *10*, 18036−18042.
(26) Wang, H.; Qi, J.; Qian, X. Electrically Tunable High Curie Temperature Two-Dimensional Ferromagnetism in van Der Waals Layered Crystals. *Appl. Phys. Lett.* **2020**, *117*, No. 083102.
(27) McGuire, M. A.; Dixit, H.; Cooper, V. R.; Sales, B. C. Coupling of Crystal Structure and Magnetism in the Layered, Ferromagnetic Insulator CrI3. *Chem. Mater.* **2015**, *27*, 612−620.

(28) McGuire, M. A. Crystal and Magnetic Structures in Layered, Transition Metal Dihalides and Trihalides. *Crystals* **2017**, *7*, 121.
(29) Goodenough, J. B. Theory of the Role of Covalence in the Perovskite-Type Manganites [La, M(II)]MnO3. *Phys. Rev.* **1955**, *100*, 564−573.
(30) Goodenough, J. B. An Interpretation of the Magnetic Properties of the Perovskite-Type Mixed Crystals La1−xSrxCoO3−λ. *J. Phys. Chem. Solids* **1958**, *6*, 287−297.
(31) Kanamori, J. Superexchange Interaction and Symmetry Properties of Electron Orbitals. *J. Phys. Chem. Solids* **1959**, *10*, 87−98.
(32) Luttinger, J. M. Fermi Surface and Some Simple Equilibrium Properties of a System of Interacting Fermions. *Phys. Rev.* **1960**, *119*, 1153−1163.
(33) Luttinger, J. M.; Ward, J. C. Ground-State Energy of a Many-Fermion System. II. *Phys. Rev.* **1960**, *118*, 1417−1427.
(34) Schedin, F.; Geim, A. K.; Morozov, S. V.; Hill, E. W.; Blake, P.; Katsnelson, M. I.; Novoselov, K. S. Detection of Individual Gas Molecules Adsorbed on Graphene. *Nat. Mater.* **2007**, *6*, 652−655.
(35) Gong, Y.; Guo, J.; Li, J.; Zhu, K.; Liao, M.; Liu, X.; Zhang, Q.; Gu, L.; Tang, L.; Feng, X.; Zhang, D.; Li, W.; Song, C.; Wang, L.; Yu, P.; Chen, X.; Wang, Y.; Yao, H.; Duan, W.; Xu, Y.; Zhang, S.-C.; Ma, X.; Xue, Q.-K.; He, K. Experimental Realization of an Intrinsic Magnetic Topological Insulator*. *Chin. Phys. Lett.* **2019**, *36*, No. 076801.
(36) Li, J.; Li, Y.; Du, S.; Wang, Z.; Gu, B.-L.; Zhang, S.-C.; He, K.; Duan, W.; Xu, Y. Intrinsic Magnetic Topological Insulators in van Der Waals Layered MnBi2Te4-Family Materials. *Sci. Adv.* **2019**, *5*, No. eaaw5685.
(37) Cai, X.; Song, T.; Wilson, N. P.; Clark, G.; He, M.; Zhang, X.; Taniguchi, T.; Watanabe, K.; Yao, W.; Xiao, D.; McGuire, M. A.; Cobden, D. H.; Xu, X. Atomically Thin CrCl3: An In-Plane Layered Antiferromagnetic Insulator. *Nano Lett.* **2019**, *19*, 3993−3998.
(38) Anderson, P. W.; Hasegawa, H. Considerations on Double Exchange. *Phys. Rev.* **1955**, *100*, 675−681.
(39) de Gennes, P.-G. Effects of Double Exchange in Magnetic Crystals. *Phys. Rev.* **1960**, *118*, 141−154.
(40) Diederich, G. M.; Cenker, J.; Ren, Y.; Fonseca, J.; Chica, D. G.; Bae, Y. J.; Zhu, X.; Roy, X.; Cao, T.; Xiao, D.; Xu, X. Tunable Interaction between Excitons and Hybridized Magnons in a Layered Semiconductor. *Nat. Nanotechnol.* **2023**, *18*, 23−28.
(41) Giannozzi, P.; Baroni, S.; Bonini, N.; Calandra, M.; Car, R.; Cavazzoni, C.; Ceresoli, D.; Chiarotti, G. L.; Cococcioni, M.; Dabo, I.; Corso, A. D.; Gironcoli, S. de; Fabris, S.; Fratesi, G.; Gebauer, R.; Gerstmann, U.; Gougoussis, C.; Kokalj, A.; Lazzeri, M.; Martin-Samos, L.; Marzari, N.; Mauri, F.; Mazzarello, R.; Paolini, S.; Pasquarello, A.; Paulatto, L.; Sbraccia, C.; Scandolo, S.; Sclauzero, G.; Seitsonen, A. P.; Smogunov, A.; Umari, P.; Wentzcovitch, R. M. QUANTUM ESPRESSO: A Modular and Open-Source Software Project for Quantum Simulations of Materials. *J. Phys.: Condens. Matter* **2009**, *21*, No. 395502.
(42) Hamann, D. R. Optimized Norm-Conserving Vanderbilt Pseudopotentials. *Phys. Rev. B* **2013**, *88*, No. 085117.
(43) Grimme, S. Semiempirical GGA-type Density Functional Constructed with a Long-Range Dispersion. *Correction. J. Comput. Chem.* **2006**, *27*, 1787−1799.
(44) Zhang, Y.; Liu, F. Maximum Asymmetry in Strain Induced Mechanical Instability of Graphene: Compression versus Tension. *Appl. Phys. Lett.* **2011**, *99*, No. 241908.
(45) Bengtsson, L. Dipole Correction for Surface Supercell Calculations. *Phys. Rev. B* **1999**, *59*, 12301−12304.

https://doi.org/10.1021/acsnano.3c07125
ACS Nano 2023, 17, 22684−22690